Enhanced visible-light photocatalytic activity of $Fe_3O_4@MoS_2@Au$ nanocomposites for methylene blue degradation through Plasmon-Induced charge transfer

Pradeep Kumar [a], Zu-Yin Deng [a], Po-Yu Tsai [a], Chin-Ya Chiu [b], Chin-Wei Lin [c], Priyanka Chaudhary [d], Yu-Ching Huang [d,e,f,*], Kuen-Lin Chen [a,b,*]

[a] *Department of Physics, National Chung Hsing University, Taichung 40227, Taiwan*
[b] *Institute of Nanoscience, National Chung Hsing University, Taichung 40227, Taiwan*
[c] *Department of Physics, National Taiwan University, Taipei 10617, Taiwan*
[d] *Department of Materials Engineering, Ming Chi University of Technology, New Taipei City 243303, Taiwan*
[e] *Biochemical Technology R&D Center, Ming Chi University of Technology, New Taipei City 243303, Taiwan*
[f] *Department of Chemical and Materials Engineering, Chang Gung University, Taoyuan 33302, Taiwan*

A B S T R A C T

In this study, we synthesized $Fe_3O_4@MoS_2@Au$ nanoparticles as a photocatalyst for the degradation of methylene blue (MB). The presence of gold nanoparticles induced Localized Surface Plasmon Resonance (LSPR), extending the absorption range into the visible light spectrum. Under green light exposure (540 nm, 8 W), the $Fe_3O_4@MoS_2@Au$ photocatalyst exhibited remarkable performance, achieving a degradation efficiency of 98.95%, outperforming $Fe_3O_4@MoS_2$, which reached 72.46%. The pseudo-first-order reaction rate constant for $Fe_3O_4@MoS_2@Au$ was 3.8×10^{-3} min^{-1}, surpassing $Fe_3O_4@MoS_2$ by 2.7 times. Additionally, $Fe_3O_4@MoS_2@Au$ demonstrated superior degradation efficiency under natural light, reaching 78% after 3 h compared to 70.2% for $Fe_3O_4@MoS_2$. To elucidate the degradation mechanism, density functional theory (DFT) based computational simulations were employed to analyze the electron charge density at each step of the degradation process. The density of state simulation revealed a shift in electron energy levels towards higher energies in $Fe_3O_4@MoS_2@Au$ compared to $Fe_3O_4@MoS_2$, thereby promoting electron transfer and enhancing the efficiency of photodegradation.

1. Introduction

The health of billions of people is worsening on a daily basis as a result of numerous contaminants in the water, which poses a significant challenge in the current scenario [1,2]. Around the world, 80 percent of municipal wastewater is dumped into untreated water bodies. Industries are responsible for releasing millions of tons of waste annually, including hazardous sludge, heavy metals, and solvents [3,4]. Water pollution poses risks to aquatic ecosystems, human health, and productive activities [5]. More than 7×10^5 tons and 1,000,000 commercial dyes have been produced annually [6]. By 2050, water consumption will triple due to population growth. Annually, more deaths of living beings are caused by polluted water than by war and all forms of violence combined. The availability of fresh water is a crucial issue that will remain important in the present and future of this rapidly growing century. Consequently, environmental remediation is a pressing concern at present. Advanced oxidation technologies (AOT) [7] are used to treat stubborn contaminants and convert them into more biodegradable compounds or mineralization into CO_2 and additional inorganic compounds for water purification [8].

Nanocomposites have good physical, chemical, and biological characteristics that can be controlled by the internal structure with interfacial interaction, which may be crucial for applicative developments in nanoelectronics, biology, and medicine [9–12]. Core-shell nanocomposite materials have attracted a lot of attention because of their distinct physical, chemical, and functional

characteristics [13]. Various techniques, such as ion doping, noble metal deposition, and nanocomposite fabrication, can be used to enhance the photocatalysis of nanomaterials [14]. However, heterojunction catalysts used in these techniques may generate secondary pollution during the photocatalytic reaction. Magnetic compound-based photocatalysis can help reduce this problem by allowing separation using an external magnet after the photocatalytic process and enabling reuse. Fe_3O_4 is a promising photocatalyst for water treatment due to its magnetic properties, low cost, recyclability, non-toxicity, and ease of modification [15]. The octahedral sites of Fe_3O_4 containing both Fe^{2+} and Fe^{3+} accelerate the mobility of electrons during ozonation [16]. In photocatalysis, a magnetic compound causes the photo-Fenton and Fenton reactions, increasing the number of radicals [17]. Therefore, Fe_3O_4 enhanced the radicals in the photocatalytic reaction.

The application of 2D materials for photocatalysts in natural light is limited due to their large band gap and low quantum yield. To address these restrictions, surface-tuning strategies like as doping and surface modification have been developed [18]. The iron oxide have been used in different application. Nowadays researchers are considering the various properties of iron oxide composite with carbonic and 2d nanomaterials such as graphene [19,20], MoS_2 [21], etc. [22,23]. The metal nanoparticles (Ag, Au, Pt) modification compounds are used to enhance the photocatalyst activity in the presence of visible light and extend the light absorption spectrum into the visible region, which is a current research hotspot [24]. Therefore, the use of sunlight (natural light) as an inexpensive and renewable energy source in photocatalytic processes has been feasible [18]. While many semiconductor materials have the potential to be used as photocatalysts for water purification, their effectiveness is often limited by a wide bandgap, a short lifetime of electron-hole pairs, and high energy demands, resulting in low catalytic efficiency [25,26]. Intrinsically, three main factors affect photocatalysis: the surface-to-volume ratio, quantum confinement, and electrodynamic interaction [27]. The surface-to-volume ratio of nanoparticles is directly proportional to the free electrons on the surface. A larger surface-to-volume ratio means more free electrons on the material surface. Therefore, a large surface-to-volume ratio can enhance the photocatalytic reaction [28]. The quantum confinement occurs due to a change in the optical bandgap [29]. The quantum confinement effect is related to the Bohr exciton radius, which is affected by the size of the semiconductor and metal nanocrystals [30]. Quantum confinement effects alter the optical, electrical, magnetic, and chemical properties of materials, making semiconductor nanocrystals highly attractive as photocatalysts due to their tunable properties [31]. The van der Waals or dispersion force, an electrodynamic interaction, can be enhanced between neighboring particles, inducing charges in the dielectric property of nanomaterials [32]. While electrodynamics also influences the local surface plasmonic resonance of nanoparticles. The strongest plasmonic electric field intensities tend to be generated in the spaces between nanoparticles due to electrodynamic principles [33]. In photocatalytic reactions, photo-Fenton and Fenton [34] reactions take place due to a magnetic compound i.e. iron oxide, which was responsible for increasing the number of radicals such as superoxide radical (O_2^-), hydroxyl radical ($\cdot OH$), singlet oxygen ($^1O_2$) and reactive oxygen species (ROS). Beynod, the surface plasmonic feature of gold nanoparticles may boost enhance the rate of photo-Fenton reaction [35,36].

Based on the previous discussion, the $Fe_3O_4@MoS_2$ and $Fe_3O_4@MoS_2@Au$ nanoparticles as photocatalysts were synthesized and studied in this work. The spherical structures of $Fe_3O_4@MoS_2$ and $Fe_3O_4@MoS_2@Au$ nanoparticles were obtained via simple synthesis processes and confirmed by using field emission scanning electron microscopy (FE-SEM). The chemical compositions of the nanoparticles were also verified by energy-dispersive X-ray spectroscopy (EDS) techniques. Furthermore, the $Fe_3O_4@MoS_2$ and $Fe_3O_4@MoS_2@Au$ nanoparticles were demonstrated to act as photocatalysts to effectively remove the methylene blue (MB) dye from water in the presence of different wavelengths of light.

2. Experimental section

The supporting file contains detailed information about the reagents and materials. Furthermore, the synthesis techniques were discussed in Section 1 of the supporting information (SI). Additionally, the specifics of photocatalysis measurements and computational analysis were described in SI Sections 2 and 3, respectively.

3. Results and discussion

3.1. Characteristics of $Fe_3O_4@MoS_2@Au$ nanoparticles

The surface morphology of nanoparticles was confirmed by the FE-SEM (JEOL JSM-7800F). The hydrothermal approach was used to successfully synthesize identical spherical-shaped Fe_3O_4 nanoparticles (Fig. 1**a, b**), and the MoS_2 was successfully deposited on the surface of Fe_3O_4 nanoparticles (Fig. 1**c, d**), resulting in a flower-like structure [37]. After treatment with PVP and $HAuCl_4$, gold nanoparticles were reduced and decorated on the surface of $Fe_3O_4@MoS_2$ nanoparticles [38]. The gold nanoparticles fully cover the particle surface to form a spherical $Fe_3O_4@MoS_2@Au$ nanoparticle (Fig. 1**e, f**). The chemical elements of $Fe_3O_4@MoS_2@Au$ were characterized by EDS of FE-SEM. The EDS mappings in Fig. 1**(g-l)** illustrate the spatial distribution of Fe (Fig. 1h), O (Fig. 1i), Mo (Fig. 1j), S (Fig. 1k), and Au(Fig. 1l) elements in the $Fe_3O_4@MoS_2@Au$ nanoparticles. The central region of the particle exhibits higher concentrations of Fe and O atoms, indicating a core-like structure. Mo and S elements align with lighter contours on the surface, while Au distribution closely follows the particle's shape. These findings support the conclusion that $Fe_3O_4@MoS_2@Au$ exhibits a layered encapsulation structure, with elemental distribution providing insights into the nanoparticle's internal composition.

The lattice space and structural parameters of $Fe_3O_4@MoS_2@Au$ nanoparticles were determined by X-ray Diffractometer (XRD) (CuK$_\alpha$ radiation). The comparative XRD spectra of $Fe_3O_4@MoS_2@Au$ nanoparticles before use and after use in photocatalysis are shown in Fig. 2 (a). The diffraction peaks of Fe_3O_4 at 35.1°, 43.5°, 53°, and 62.6° can be attributed to the planes of (3 1 1), (4 0 0), (4 2 2), and (4 4 0) respectively, and were compared and analyzed with the JCPDS file No. 65-3107. The diffraction peaks of MoS_2 were found at positions 35.11°, 44.7°, 56.78°, and 62.6°, with the planes of (1 0 2), (0 0 6), (1 0 6), and (1 0 7) respectively, and were compared and analyzed with the JCPDS file No. 06-0097. The presence of Au was confirmed by comparing and analyzing the diffraction peaks with the JCPDS file No. 04-0784, where the peaks at positions 37.7°, and 64.4° with the planes of (1 1 1), and (2 2 0) respectively, were observed. The XRD peaks obtained for both scenarios (original and recycled materials) were found at identical positions, indicating the stability of $Fe_3O_4@MoS_2@Au$ nanoparticles. This observation suggests that the nanoparticles remained unchanged and did not undergo any reactions with methylene blue during the degradation process. The sharpness and high intensity of XRD peaks indicate the high crystallinity of $Fe_3O_4@MoS_2@Au$ nanoparticles. The XRD signals of the recycled material exhibit a slight broadening, which may result from minor damage to the crystallinity of the sample during the recycling and cleaning process [39]. The transmission electron microscope (TEM) results revealed the spherical morphology of $Fe_3O_4@MoS_2@Au$, as shown in Fig. 2**(b)**. The surface of Fe_3O_4 was covered with MoS_2, while MoS_2 on the iron oxide was covered with gold, as shown in Fig. 2**(c)**. The structure description of the synthesized core–shell nanoparticles is given in Fig. 2**(d)**. MoS_2, and Au exhibit crystal faces with (0 0 2) and (1 1 1) orientations, accompanied by corresponding d-spacing values of 0.64 nm, and 0.269 nm. Otherwise, clear lattice lines cannot be observed by TEM for Fe_3O_4 deep in the structure.

The absorption behaviors of the synthesized materials were analyzed with the UV–Vis spectrometer (JASCO U-550). Fig. 3**(a)** illustrates that the $Fe_3O_4@MoS_2$ exhibits three MoS_2 peaks [37,40] at 385 nm, 445 nm, and 696 nm. Moreover, $Fe_3O_4@MoS_2@Au$ nanoparticles possess a broad

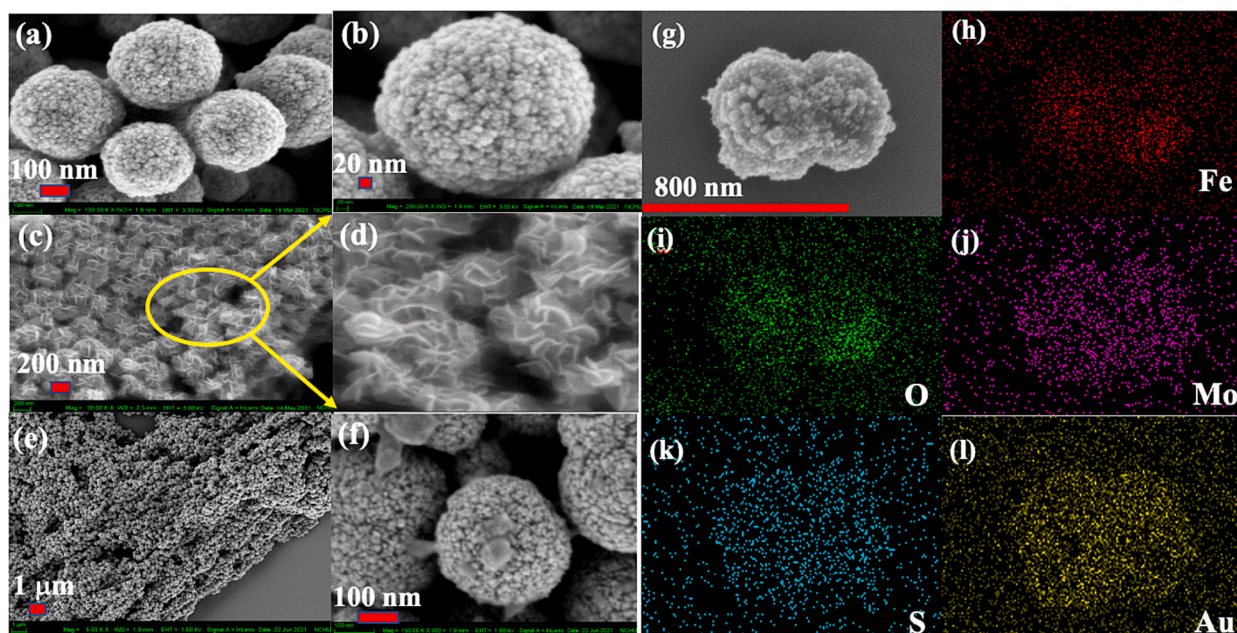**Fig. 1.** The morphological characteristics of Fe_3O_4 (a, b), $Fe_3O_4@MoS_2$ (c, d), and $Fe_3O_4@MoS_2@Au$ (e, f) were examined using FE-SEM. EDS mapping analysis of $Fe_3O_4@MoS_2@Au$ by FE-SEM (g-l).
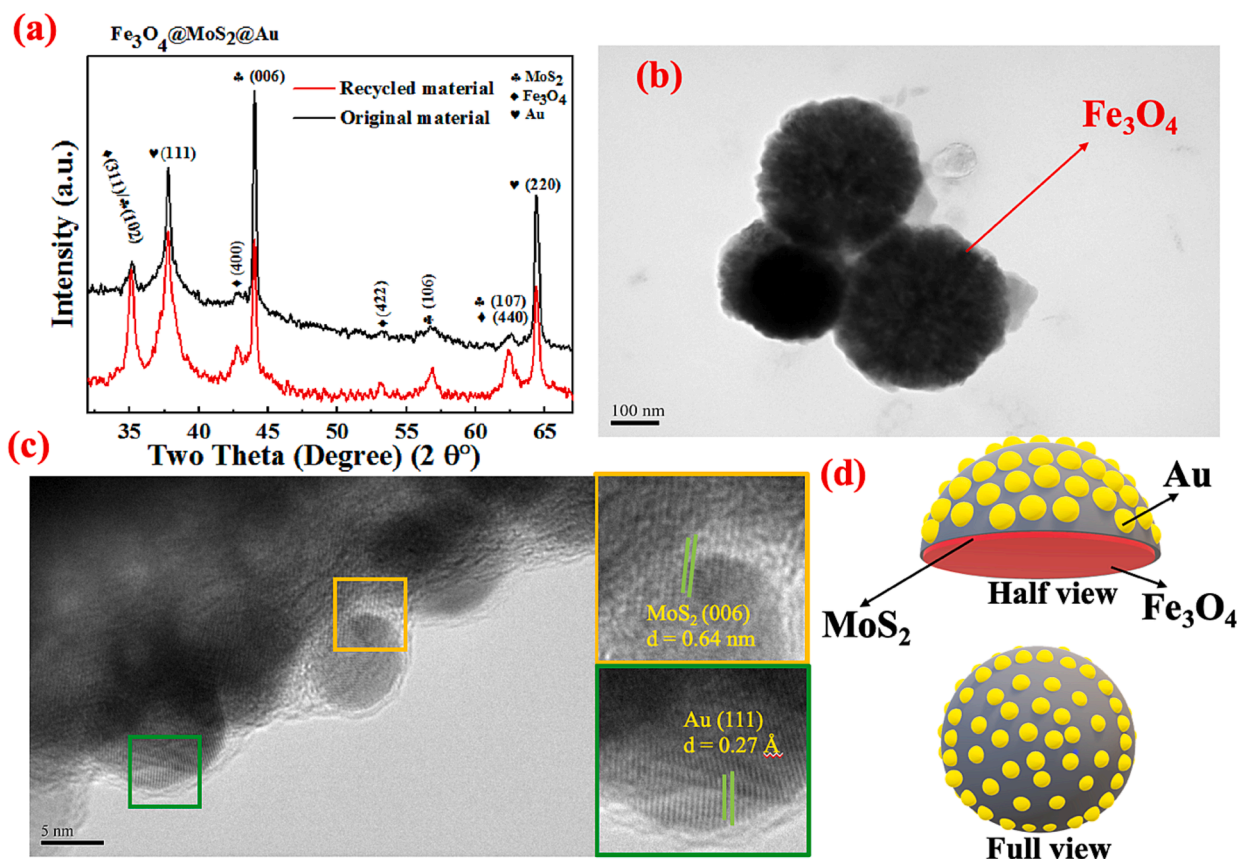

Fig. 2. (a) XRD spectra of original and recycled materials, and (b, c) high-magnification cross-section TEM images of $Fe_3O_4@MoS_2@Au$. (d) Schematic structure of $Fe_3O_4@MoS_2@Au$ nanoparticles.

absorption spectrum in the range of 400 nm–850 nm, and a specific absorption peak of MoS_2 was revealed at 681 nm. This broad absorption occurred because of the plasmonic behavior of Au. The absorption spectra of $Fe_3O_4@MoS_2@Au$ showed a redshift in the Au peak, which can be attributed to the surface plasmonic behavior of the gold shell [31,32]. The atomic vibrations and structural properties of the synthesized materials were studied using Raman spectroscopy (NANOSCOPE/ NS220). The Raman active vibration modes of $Fe_3O_4@MoS_2@Au$ and
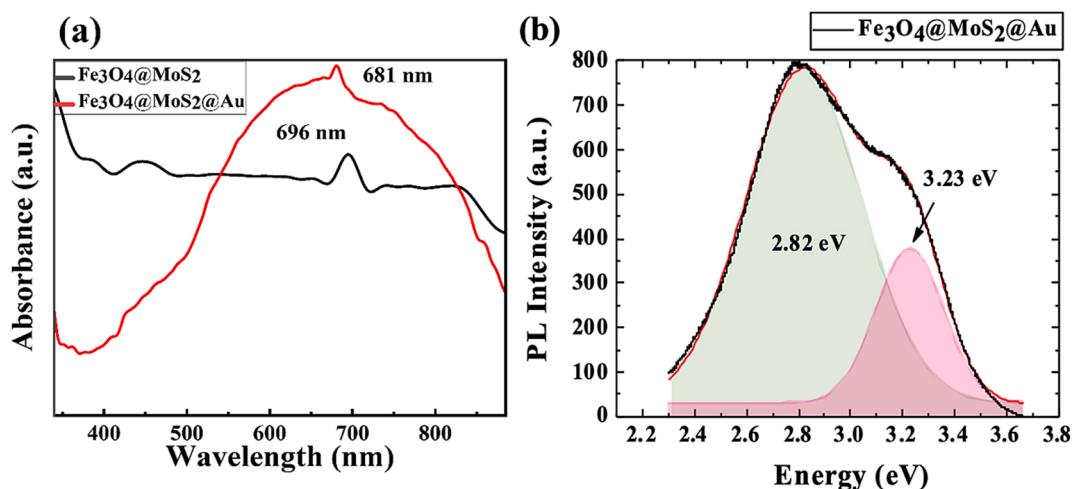
Fig. 3. (a) Optical properties of Fe$_3$O$_4$@MoS$_2$@Au and Fe$_3$O$_4$@MoS$_2$ at room temperature. UV light absorbance spectra. (b) PL spectra of Fe$_3$O$_4$@MoS$_2$@Au.

Fe$_3$O$_4$@MoS$_2$ nanoparticles were presented in **SI**-Fig. 2**(a)** The Raman vibration of Fe$_3$O$_4$@MoS$_2$@Au was observed to be higher intensity than that of Fe$_3$O$_4$@MoS$_2$. The Raman active phonon modes for MoS$_2$, which were observed, included 169 cm^{-1}(A$_{1g}$-LA(M)), 380 cm^{-1} (E_{2g}^1), 441 cm^{-1} (2LA(M)). Meanwhile, the peaks for iron oxide were recorded at 290 cm^{-1}(T$_{1g}$), 674 cm^{-1}(A$_{1g}$), and 1387 cm^{-1}(2LA(M)) [36]. The peak around 1596 cm^{-1} belongs to Au enhancement [36,41–43]. The MoS$_2$ Raman signals seem to be a little weak because it was fully covered by Au nanoparticles. The JASCO-FT-IR 4600 instrument was used to record the Fourier transform infrared (FTIR) spectrum. **SI**-Fig. 2**(b)** illustrates the FTIR spectrum of Fe$_3$O$_4$@MoS$_2$@Au and Fe$_3$O$_4$@MoS$_2$. Analysis of the FT-IR vibrations of Fe$_3$O$_4$@MoS$_2$@Au revealed that peaks between 350 and 430 cm^{-1} correspond to Fe-O stretching, while those at 458 cm^{-1} and 609 cm^{-1} correspond to Mo-S vibrations [36,44,45]. However, the peaks at 552 cm^{-1}, 740 cm^{-1}, and around 969 cm^{-1} are

attributed to Fe-O stretching and bending vibrations. Nonetheless, the vibration 1107 cm^{-1} is determined to be the stretching vibrations of the MoS$_2$.

To investigate the luminescence properties of Fe$_3$O$_4$@MoS$_2$@Au nanoparticles, photoluminescence (PL) measurement was conducted with an excitation wavelength of 352 nm, as shown in Fig. 3**(b)**. Two luminescence bands were observed, with the stronger one at 2.82 eV (440 nm) and the other at 3.23 eV (384 nm). The spectrum at 3.23 eV corresponds to the bandgap of iron oxide [46], while the signal at 2.82 eV arises from nano-sized gold [47]. Due to the signal amplification generated by surface plasmon resonance, signal overlap occurs, resulting in a broader bandwidth. This phenomenon implies that the presence of nano-sized gold facilitates electron transitions at lower energy levels. Consequently, we deduce that the incorporation of nano-sized gold into the Fe$_3$O$_4$@MoS$_2$ material enables photocatalytic processes with light

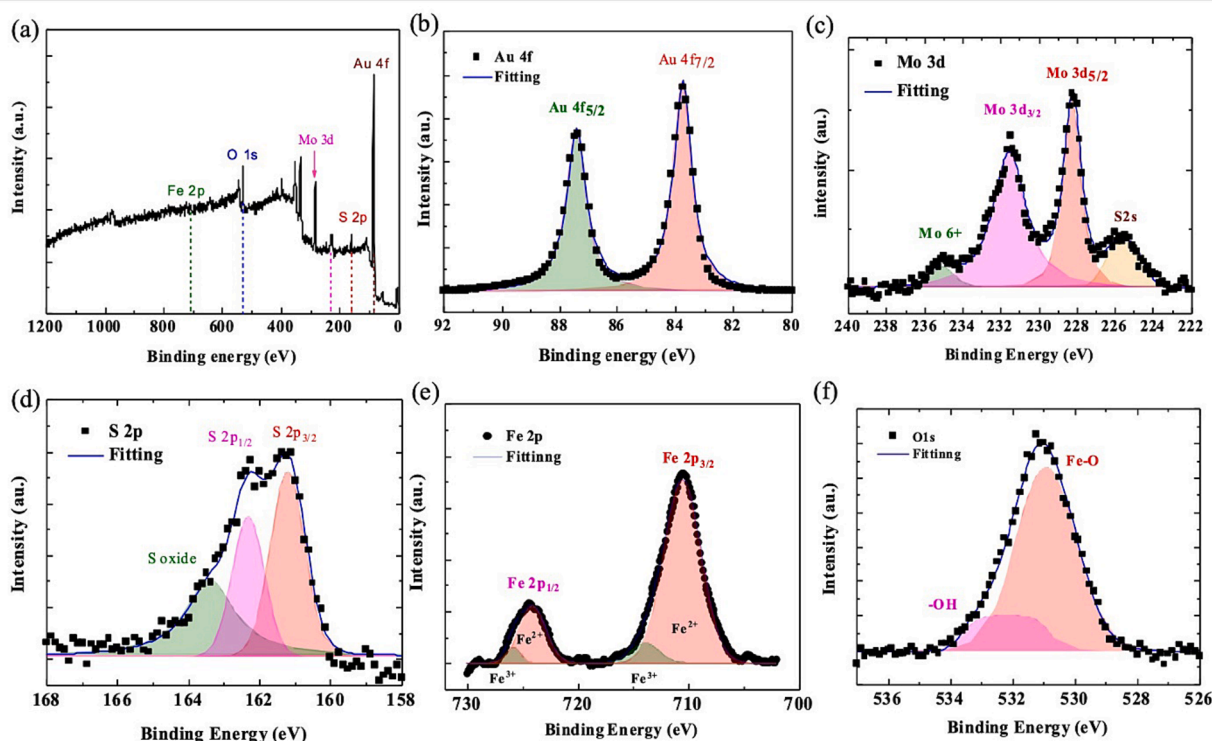**Fig. 4.** XPS spectra of Fe$_3$O$_4$@MoS$_2$@Au. (a) a full-scan spectrum of Fe$_3$O$_4$@MoS$_2$@Au. (b-e) high-resolution spectra of (b) Au, (c) Mo, (d) S, (e) Fe, and (f) O.

sources of longer wavelengths, thereby yielding energy-efficient outcomes. The energy levels of several elements were analyzed using X-ray photoelectron spectroscopy (XPS) spectra as shown in Fig. 4 and compared with the literature; the results showed consistency with metallic gold, MoS_2, and Fe_3O_4. The signals for Au at 87.4 eV ($4f_{5/2}$) and 83.75 eV ($4f_{7/2}$) match the energy distribution of metallic gold, indicating that the formation of gold nanoparticles did not involve chemical bonding with other materials [48]. The binding energy with the highest peaks of Mo was observed at 228.3 eV ($3d_{5/2}$) and 231.6 eV ($3d_{3/2}$), whereas S $2p_{1/2}$ and 2s have excited states at 161.2 eV and 226 eV, respectively [49]. The O_{1s} peaks appear at 530.7 eV as the main peak representing the bonding energy of Fe-O, and a smaller peak at 531.8 eV corresponding to surface-adsorbed OH functional groups [50]. The signals for Fe and O also align with Fe_3O_4, with peaks at 710.7 eV and 724 eV for Fe $2p_{3/2}$ and Fe $2p_{1/2}$, respectively [36,51]. The asymmetric peak shapes [51] indicate a distribution of charges, including Fe^{3+} and Fe^{2+}.

3.2. Photocatalysis characterization

In the following experiment, the photodegradation of MB was performed under UV light (8 W) and green light (8 W) at neutral conditions (pH = 7) and room temperature (300 K). The UV–Vis absorption spectra of MB during its photodegradation by $Fe_3O_4@MoS_2$ and $Fe_3O_4@MoS_2@Au$ nanoparticles were shown in SI-Fig. 3(a-d). The photocatalytic characterizations of $Fe_3O_4@MoS_2$ and $Fe_3O_4@MoS_2@Au$ nanoparticles were analyzed based on the major absorbance peak of MB at 661 nm. The photocatalytic kinetics of $Fe_3O_4@MoS_2$ and $Fe_3O_4@MoS_2@Au$ nanoparticles were illustrated in Fig. 5, showcasing the findings of the degradation ratio, efficiency, and pseudo-first-order reaction constant. After 9 hrs of exposure to UV light, the absorption peak of MB at 661 nm decreased more significantly in the $Fe_3O_4@MoS_2$ treatment than in the

$Fe_3O_4@MoS_2@Au$ treatment. The calculated MB degradation efficiencies of $Fe_3O_4@MoS_2$ and $Fe_3O_4@MoS_2@Au$ were 96.57 % and 79.75 %, respectively (Fig. 5a). Moreover, the kinetic properties of the MB degradation followed the pseudo-first-order reaction (Fig. 5b). The experiment results showed that the concentration ratio of MB was only 0.01 after the 9 hrs treatment of $Fe_3O_4@MoS_2$, which was 27 times less than that of the treatment of $Fe_3O_4@MoS_2@Au$. The pseudo-first-order reaction constant for the $Fe_3O_4@MoS_2$ treatment was 3.75×10^{-3} min^{-1}, which was 1.73 times higher than the $Fe_3O_4@MoS_2@Au$ treatment. The results suggest that no reaction occurred between MB and photocatalysis. Under UV exposure, $Fe_3O_4@MoS_2$ nanoparticles have better degradation efficiency for MB. However, the use of UV treatment may not be an environmentally friendly solution for water pollution treatment. The UV light of type A in the range of 315–400 nm is also responsible for skin cancer, retinal burn, etc. [52]. Compared with UV light, the use of visible light in photocatalysis can be more environmentally friendly and energy-saving. The plasmonic property of gold can be effectively excited by the green light, and thus the photocatalytic performance of $Fe_3O_4@MoS_2@Au$ nanoparticles was enhanced. In contrast, the $Fe_3O_4@MoS_2@Au$ treatment exhibited a more pronounced decrease in the absorbance peak of MB at 661 nm compared to $Fe_3O_4@MoS_2$ under green light exposure, as shown in Fig. 5(c,d). After 9 hrs of exposure to green light, the concentration ratios of MB were 0.27 and 0.01 for $Fe_3O_4@MoS_2$ and $Fe_3O_4@MoS_2@Au$ treatments, respectively (Fig. 5c). Meanwhile, $Fe_3O_4@MoS_2@Au$ and $Fe_3O_4@MoS_2$ exhibited degradation efficiencies of 98.97% and 72.78 % for MB, respectively. The behavior of the pseudo-first-order [36] reaction constant rate was linear as shown in Fig. 5(d). It also indicated that there was no reaction between MB and photocatalysis. The pseudo-first-order reaction constant for $Fe_3O_4@MoS_2@Au$ under green light was 3.8×10^{-3} min^{-1}, which was 2.7 times higher than that of $Fe_3O_4@MoS_2$. The
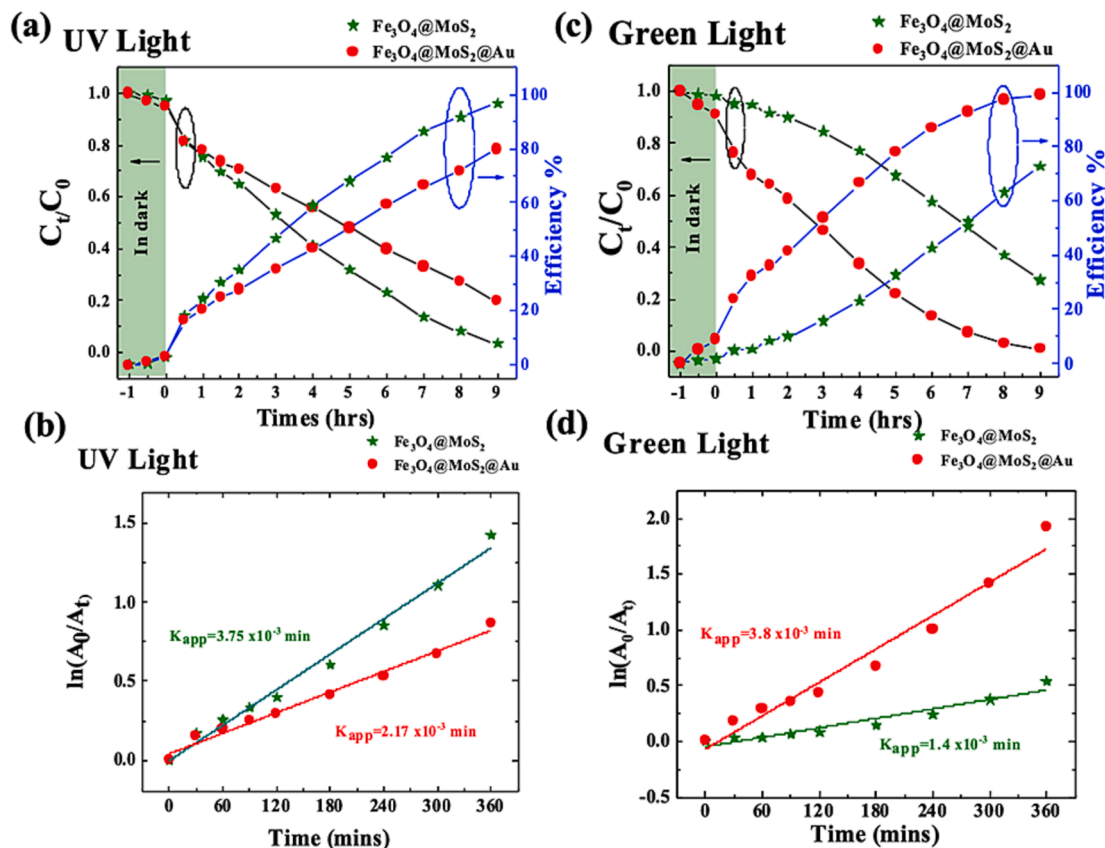

Fig. 5. Photocatalytic degradation of MB. Concentration ratio C_t/C and degradation efficiency (**a, c**); pseudo-first-order reaction rate constant (min^{-1}) for the absorbance peak of MB at 661 nm with time (**b, d**).

experimental data indicates that the photocatalytic activity of $Fe_3O_4@MoS_2@Au$ nanoparticles was superior to that of $Fe_3O_4@MoS_2$ under green light. Additionally, it achieved equivalent degradation efficiencies under green light photocatalytic conditions as $Fe_3O_4@MoS_2$ under UV light, demonstrating its remarkable practicability. The recycling of the $Fe_3O_4@MoS_2@Au$ nanoparticles has been performed three times, as illustrated in **SI**-Fig. 4, and has been thoroughly described in the supporting information. A small difference in the absorbance ratio (**SI**-Fig. 4**a**) and efficiency (**SI**-Fig. 4**b**) was seen in the original to 3rd round of the recycling test. During the original to 3rd round, the degradation efficiencies were calculated as 85.74%, 84.3%, 82.6%, and 79.23% respectively after 5 hrs. These results indicated that this material has good stability for photocatalytic and can be used for the recycling process.

Greenlight is the main component of natural sunlight. Therefore, an experiment was also conducted on the morning of a sunny day under natural sunlight to investigate the photocatalytic properties of $Fe_3O_4@MoS_2@Au$ and $Fe_3O_4@MoS_2$ nanoparticles in degrading MB. To simulate the common conditions, this experiment was conducted on a table next to an unobstructed window one morning. The kinetic behavior such as absorbance, efficiency, degradation ratio, and the pseudo-first-order reaction constant curves of the photocatalysts have been shown in Fig. 6. $Fe_3O_4@MoS_2@Au$ exhibits better photocatalytic activities than $Fe_3O_4@MoS_2$ under exposure to natural sunlight. Within 3 hrs, the degradation efficiency of $Fe_3O_4@MoS_2@Au$ and $Fe_3O_4@MoS_2$ for MB reached 78.0% and 70.2%, respectively (Fig. 6**a**). The pseudo-first-order reaction constant for $Fe_3O_4@MoS_2@Au$ under sunlight was 6.3×10^{-3} min^{-1}, which was 1.6 times higher than that of $Fe_3O_4@MoS_2$ (Fig. 6**b**). The experimental data indicated that the photocatalytic performance of $Fe_3O_4@MoS_2@Au$ nanoparticles was better than that of $Fe_3O_4@MoS_2$ under natural sunlight. As shown in Table 1., different heterojunction-based photocatalysis has been focused on in order to increase the degradation efficiency of organic compounds.

3.3. Charge transfer analysis based theoretical analysis

To investigate the impact of gold nanoparticles on $Fe_3O_4@MoS_2$, simulation experiments were conducted using VASP 6.1.1 software, as shown in Fig. 7. In this model, crystalline Fe_3O_4 was combined with a two-dimensional MoS_2 material. Subsequently, a comparative analysis of the changes in electronic charge resulting from the integration of two interconnected gold nanoparticle structures was performed, as depicted in Fig. 7**(a).**

Fig. 7**(b)** depicts the variations of charge distribution for each atom after the addition of gold atoms. The red color represents positive

Table 1

A comparative study of photocatalytic capabilities for MB dye degradation described in the literature.

Composition Name	Source	Degradation efficiency %	Reference
$C_3N_4/Fe_3O_4/Bi_2WO_6/$ Bi_2S_3	140 W LED	99.8	[53]
$Fe_3O_4@Ti-PDA$	Xenon lamp reactor (PLS-SXE300)	92.4	[54]
ZnO/Fe_3O_4	UV light	99.7	[55]
$G/Co/Fe_3O_4$	UV light	78	[56]
$Fe_3O_4/PPy/C$	–	95.9	[57]
MoS_2	20 W halogen lamp	98	[58]
$Fe_3O_4@MoS_2$	UV light/Green light	96.57/72.46	This work
$Fe_3O_4@MoS_2@Au$	UV light/Green light	79.74/98.95	This work

charges, whereas the light blue color represents negative charges. The charge distribution and charge difference depiction demonstrate that the introduction of gold nanoparticle configurations causes observable electron migration from the outermost layer of gold and MoS_2 toward the internal Fe_3O_4 matrix. Consequently, this results in an enhanced positive charge distribution (indicated in red) within the MoS_2 constituents, while simultaneously creating an additional negative charge reservoir (indicated in light blue) within the Fe_3O_4 substrate. According to electron valence calculations, iron atoms gained an average of 0.58 electrons due to the presence of the gold structure. Whereas, oxygen atoms gain 2.06 electrons. In MoS_2 materials, Mo atoms lose 2.05 electrons, and S atoms lose 0.09 electrons. The electronic density of state (DOS) of $Fe_3O_4@MoS_2$ and $Fe_3O_4@MoS_2@Au$ has been compared as shown in Fig. 7**(c)**. It was observed that the inclusion of gold nanoparticles to the outer layer of the $Fe_3O_4@MoS_2$ nanoparticles increased entire electron energy, causing their distribution to shift towards higher energy levels, as seen in Fig. 7**(c)**. This observation suggests that the sample, when compared to its state before the addition of gold nanoparticles, exhibits a higher electron affinity and enhanced chemical reactivity [59].

3.4. Mechanism

The photocatalytic mechanism of $Fe_3O_4@MoS_2@Au$ with MB in dark and light has been illustrated in Fig. 8. The molecular structure of MB is given in reference [60]. The possible reaction mechanisms during the photocatalytic processes were listed in equations 1 to 9 [36,61–65]. Oxidizing radicals and ROS were generated during a reaction due to the interaction of light and oxygen ions in the presence of moisture [66]. Superoxide radical (O_2^-), hydroxyl radical ($\cdot OH$), singlet oxygen ($^1O_2$)
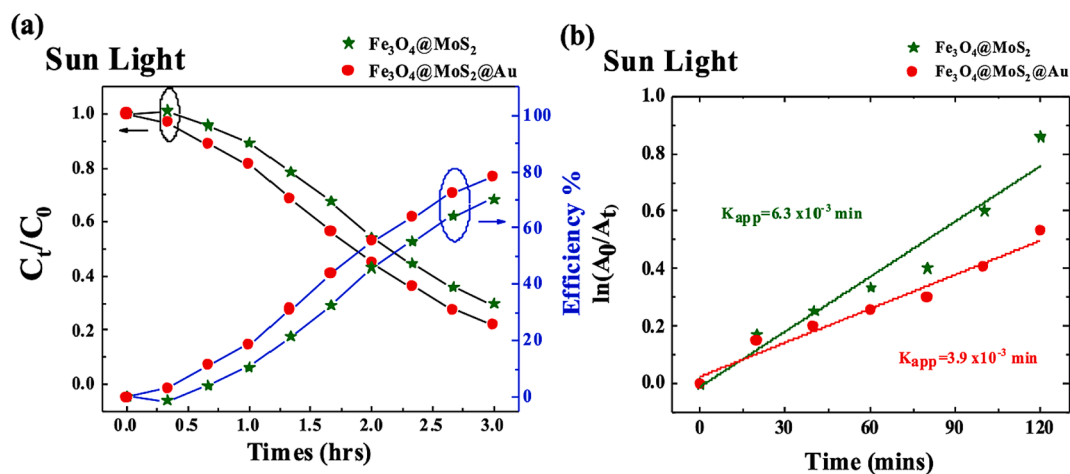
Fig. 6. Photocatalytic degradation of MB by $Fe_3O_4@MoS_2@Au$ and $Fe_3O_4@MoS_2$ nanoparticles in the presence of natural light. Concentration ratio C_t/C_o and degradation efficiency **(a)**; pseudo-first-order reaction rate constant (min^{-1}) for the absorbance peak of MB at 661 nm with time **(b)**.
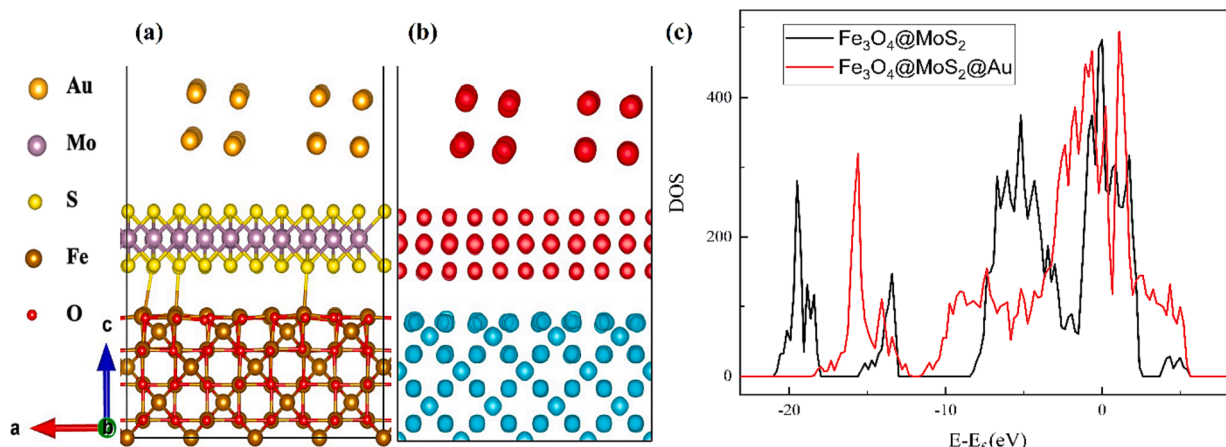
Fig. 7. (a) Computationally model of $Fe_3O_4@MoS_2@Au$ structure. (b) Variations of charge distribution for each atom after the addition of gold atoms. (c) DOS comparison between $Fe_3O_4@MoS_2$ and $Fe_3O_4@MoS_2@Au$.
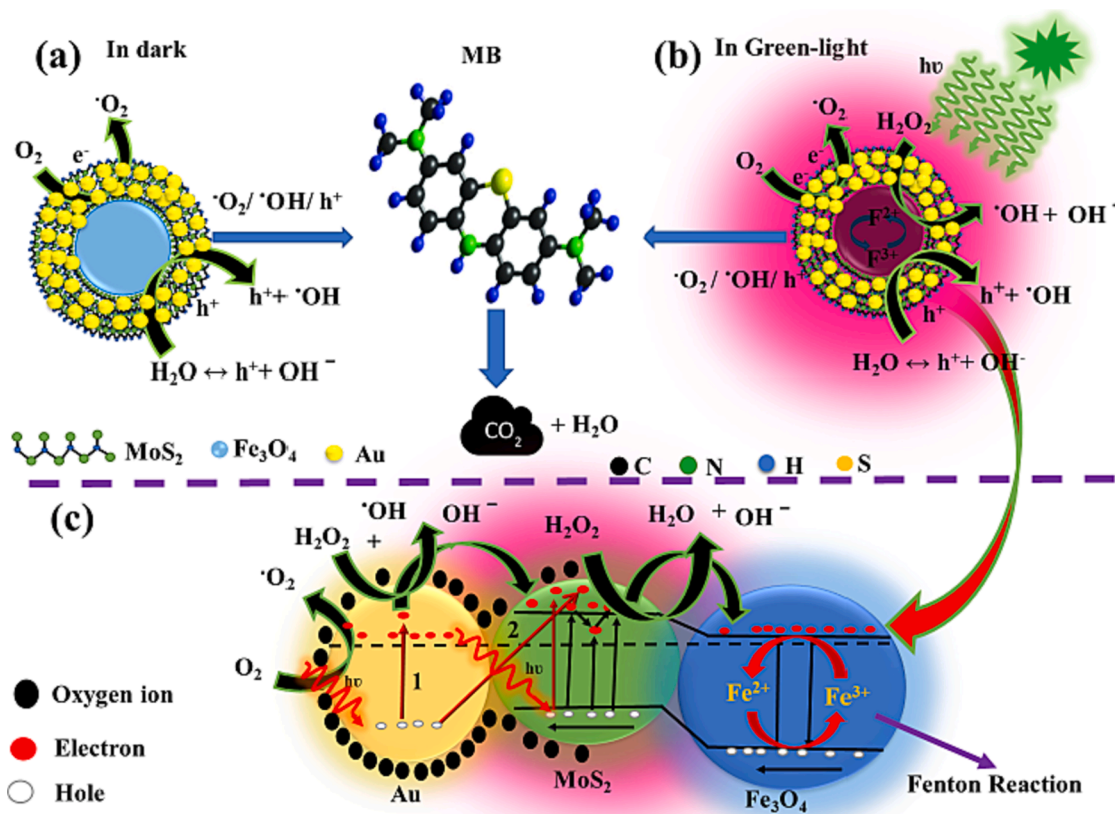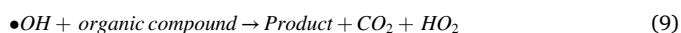

Fig. 8. Degradation mechanism of $Fe_3O_4@MoS_2@Au$ nanoparticle in dark and green light. (For interpretation of the references to color in this figure legend, the reader is referred to the web version of this article.)

and ROS [36] are highly reactive molecules in comparison to oxygen molecules. The degradation rate of the reaction was dominated by the number of generated radicals [36]. Here, Au and MoS_2 played an important role to generate the radicals on a large scale. Nonetheless, Au has plasmonic behavior at a green light and has an important role to enhance the degradation of MB. Gold-based catalysts can stimulate the breakdown of H_2O_2 into $\cdot OH$ [67]. Under dark conditions, a small number of free charges on the surface of $Fe_3O_4@MoS_2@Au$ interact with oxygen and water molecules, leading to the generation of radicals, as illustrated in Fig. 8(a). Therefore, the degradation of MB was observed in the dark. The degradation of MB was halted when all free-charge carriers participate in the reaction, leading to a so-called

adsorption–desorption equilibrium. At the equilibrium state in the dark, small Schottky barriers were formed due to the contact of Au and MoS_2 [67], and we speculate that it hinders the movement of electrons from the Au to the internal material. Therefore, the degradation rate is very small in the dark. As well as the light was opened, then Au nanoparticles exhibited the localized surface plasmon resonance (LSPR) effect and released hot electrons quickly, which affect the mobility of charge carriers in the Fe_3O_4 [68] and MoS_2 (Fig. 8b and c). This phenomenon led to the excitation of "hot electrons" through LSPR, which subsequently moved to the outer surface of the particle, a process known as plasmon-induced hot-electron transfer (PHET) [55]. During PHET, a plasmon decays into a hot electron-hole pair within the metal through Landau

damping, followed by the transfer of the hot electron to adjacent semiconductors. These excited electrons accumulated on the outer surface of Au (way 1) and also migrated to the conduction band of MoS₂ from Au (way 2) [26]. Additionally, the plasmon-induced interfacial charge-transfer transition (PICTT) effect also facilitated the transfer of hot electrons to the conduction band of MoS₂ [55].

Meanwhile, MoS₂ also gets energy from the light and generates electrons and holes (Eq. 1). As a consequence, the CB of MoS₂ accumulates a large number of electrons, and the surplus electrons are subsequently transferred to the CB of Fe₃O₄. From the aspect of catalyzation, the PHET electrons on the particle surface quickly react with oxygen and H₂O₂ to generate a large number of ROS. The excess electrons on the CB of Fe₃O₄ via PICTT also enhance the Fenton reaction [18], which is the so-called photo-Fenton effect [69,70]. The Fenton effect is an effective way to produce highly reactive hydroxyl radicals (·OH) [69]. In summary, the Fe₃O₄@MoS₂@Au nanoparticles can efficiently produce a large number of ROS, because they can simultaneously trigger LSPR, PHET, and PICCT effects. ROS is known as the potential substance for destroying organic pollutants in wastewater.

$$MoS_2 + h\nu \rightarrow MoS_2 + h^+ + e^- \tag{1}$$

$$Au \rightarrow Au^+ + e^- \tag{2}$$

$$Fe^{2+} \leftrightarrow Fe^{3+} + e^- \tag{3}$$

$$O_2 + e^- \rightarrow O_2^- \tag{4}$$

$$H_2O_2 + e^- \rightarrow \bullet OH + OH^- \tag{5}$$

$$H_2O \leftrightarrow H^+ + OH^- \leftrightarrow \bullet OH + \bullet h^+ \tag{6}$$

$$2 \bullet OH + 2H_2O_2 \rightarrow 2 \bullet HO_2 + 2H_2O \tag{7}$$

$$\bullet HO_2 \rightarrow H^+ + O_2^- \tag{8}$$

$$\bullet OH + organic\ compound \rightarrow Product + CO_2 + HO_2 \tag{9}$$

To understand the role of ROS in charge transfer, we referred to the work of Wang et al. [62] and employed simulations to investigate the molecular charges and distribution changes during the photodegradation of MB. Fig. 9 shows the molecular charge distribution during each degradation pathway of the MB. MB gradually decomposes into shorter-chain molecules with lower toxicity, ultimately forming the end products CO₂ and H₂O. In every degradation step hydroxyl radical (·OH) reacts with carbonic molecules and continuously degrades it until the final step. From the simulation results, it can be observed that in the pristine MB molecule, the charges are mainly concentrated on the chlorine and nitrogen atoms. However, with the assistance of ROS, the charge distribution of the molecule gradually shifts towards the oxygen and sulfur atoms, causing certain bonds to break and leading to the gradual decomposition of the MB molecule. It can be understood that the photocatalysis efficiency is mainly dominated by the electron charge density [71], and ROS is the key to drive the redistribution of molecular charge.

3.5. The role of H₂O₂

From the reaction equation, it can be observed that the hydroxyl radicals (·OH) generated from the decomposition of H₂O₂ play a crucial role in the degradation process of MB. To investigate the effect of H₂O₂ during the photocatalysis of Fe₃O₄@MoS₂@Au, the degradation of the MB experiment was conducted under the exposure of green light. From the experimental results as illustrated in **SI**-Fig. 5, it can be observed that in the reaction without the addition of H₂O₂ for the 7 h, the concentration of MB was only reduced by approximately 36%. In contrast, with the addition of 1 mL of H₂O₂ (35% v/v), the degradation efficiency
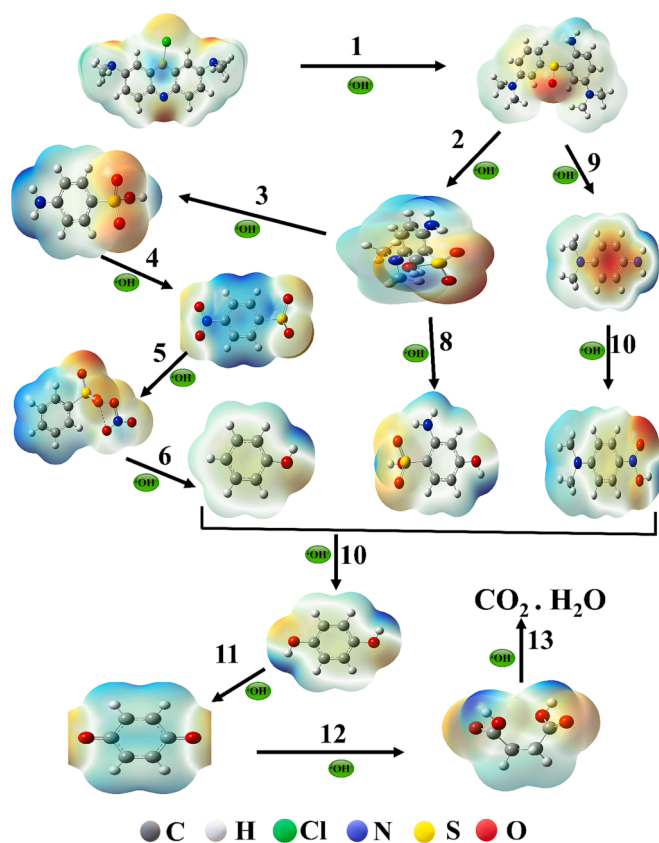

Fig. 9. Degradation pathways of MB depicted with the electron surface density from the total SCF density (isovalue = 0.02 and 0.0004) mapped with ESP. The color scale ranging from higher positive values to negative values is represented by the blue, green, yellow, and red regions. (For interpretation of the references to color in this figure legend, the reader is referred to the web version of this article.)

significantly improved, and the concentration of MB decreased by 93% within 7 h. Furthermore, it can be also observed that, with the addition of H₂O₂, there is a noticeable accelerating trend in the photodegradation rate of MB after illumination. Conversely, in the absence of H₂O₂, there is no apparent acceleration in the photodegradation rate of MB after illumination. This experimental result indicates that H₂O₂ plays a crucial role as a precursor for generating hydroxyl radicals (·OH) throughout the entire photocatalytic process. It is also a key factor influencing the overall photocatalytic efficiency.

4. Conclusion

In this study, we successfully employed gold nanoparticle-modified Fe₃O₄@MoS₂ for efficient MB photodegradation under low-energy green light conditions. We synthesized Fe₃O₄@MoS₂@Au core–shell nanoparticles by modifying the surface of hydrothermally synthesized Fe₃O₄@MoS₂ with gold nanoparticles using the reduction method. FE-SEM analysis demonstrated that Fe₃O₄@MoS₂@Au has a spherical configuration. Our results indicate that Fe₃O₄@MoS₂ nanoparticles are more active in UV light for the degradation of MB in wastewater, exhibiting an efficiency of 96.57%, which was 1.21 times higher than Fe₃O₄@MoS₂@Au nanoparticles within 9 hrs. Furthermore, we found that Fe₃O₄@MoS₂@Au exhibits better photocatalytic activity for the degradation of MB at longer wavelengths than UV light. The degradation efficiency of Fe₃O₄@MoS₂@Au was 1.36 times higher than Fe₃O₄@-MoS₂, with a value of 98.97% in the presence of green light. A linear Pseudo-first-order reaction rate constant curve was observed, indicating that Fe₃O₄@MoS₂@Au was inactive with MB. We calculated a K_{app}

pseudo-first-order reaction rate constant of 3.8×10^{-3} min^{-1} for $Fe_3O_4@MoS_2@Au$ nanoparticle under green light, which was 2.7 times higher than the value of K_{app} of $Fe_3O_4@MoS_2$ nanoparticle. We also found that $Fe_3O_4@MoS_2@Au$ exhibited a degradation efficiency of 78% in natural light, which was 1.1 times higher than $Fe_3O_4@MoS_2$ after 3 hrs. The DFT computational results demonstrate that the LSPR of gold nanoparticles amplifies the charge transfer from the external Au to the internal Fe_3O_4, resulting in an enhanced degradation efficiency. The introduction of plasmonic gold nanoparticles causes a shift in the DOS of material towards higher energy levels, inducing a more active chemical reactivity in $Fe_3O_4@MoS_2@Au$ samples, thereby generating radicals more efficiently. In conclusion, the $Fe_3O_4@MoS_2@Au$ nanoparticles exhibit exceptional solar-driven photocatalytic performance for degrading MB. The excellent solar light harvesting ability, coupled with the magnetic recyclability of this nanocomposite, signifies its immense potential as an eco-friendly and sustainable photocatalyst for practical water purification.

CRediT authorship contribution statement

Pradeep Kumar: Writing – review & editing, Writing – original draft, Visualization, Validation, Software, Methodology, Investigation, Formal analysis, Data curation. **Zu-Yin Deng:** Writing – review & editing, Visualization, Validation, Software, Investigation, Formal analysis, Data curation. **Po-Yu Tsai:** Visualization, Validation, Methodology, Investigation, Formal analysis, Data curation. **Chin-Ya Chiu:** Investigation, Formal analysis, Data curation. **Chin-Wei Lin:** Writing – review & editing, Investigation, Formal analysis. **Priyanka Chaudhary:** Writing – review & editing, Investigation. **Yu-Ching Huang:** Writing – review & editing, Validation, Supervision, Resources, Investigation, Funding acquisition. **Kuen-Lin Chen:** Writing – review & editing, Writing – original draft, Visualization, Validation, Supervision, Resources, Project administration, Methodology, Investigation, Funding acquisition, Formal analysis, Data curation, Conceptualization.

Declaration of competing interest

The authors declare that they have no known competing financial interests or personal relationships that could have appeared to influence the work reported in this paper.

Data availability

Data will be made available on request.

Acknowledgments

Appendix A. Supplementary data

Supplementary data to this article can be found online at https://doi.org/10.1016/j.seppur.2024.126988.

References

[1] D. Kanakaraju, A. Chandrasekaran, Recent advances in TiO₂/ZnS-based binary and ternary photocatalysts for the degradation of organic pollutants, Sci. Total Environ. 868 (2023) 161525, https://doi.org/10.1016/j.scitotenv.2023.161525.

[2] F. Guo, M. Li, H. Ren, X. Huang, W. Hou, C. Wang, W. Shi, C. Lu, Fabrication of P-n CuBi₂O₄/MoS₂ heterojunction with nanosheets-on-microrods structure for enhanced photocatalytic activity towards tetracycline degradation, Appl. Surf. Sci. 491 (2019) 88–94, https://doi.org/10.1016/j.apsusc.2019.06.158.

[3] M.Z. Uddin, K.K. Saha, M. Moniruzzaman, M.M. Rahman, M. Ahmed, M.M. H. Oliver, Estimation of subsurface pollutant load and its seasonal variation in an irrigation channel: Pollution load in irrigation channel, EJFOOD 4 (6) (2022) 54–61, https://doi.org/10.24018/ejfood.2022.4.6.606.

[4] C. Lu, L. Gao, S. Yin, F. Guo, C. Wang, D. Li, Fabrication of P-n MoS₂/BiOBr heterojunction with few-layered structure for enhanced photocatalytic activity toward tetracycline degradation, DWT 207 (2020) 341–351, https://doi.org/10.5004/dwt.2020.26393.

[5] M. Kumar, S. Ambika, A. Hassani, P.V. Nidheesh, Waste to catalyst: Role of agricultural waste in water and wastewater treatment, Sci. Total Environ. 858 (2023) 159762, https://doi.org/10.1016/j.scitotenv.2022.159762.

[6] F.M.D. Chequer, G.A.R.de. Oliveira, E.R.A. Ferraz, J.C. Cardoso, M.V.B. Zanoni, D. P.de Oliveira, F.M.D. Chequer, G.A.R.de Oliveira, E.R.A. Ferraz, J.C. Cardoso, M.V. B. Zanoni, D.P.de Oliveira, Textile dyes: Dyeing process and environmental impact, IntechOpen (2013), https://doi.org/10.5772/53659.

[7] T.B. Nguyen, R. Doong, C.P. Huang, C.-W. Chen, C.-D. Dong, Activation of persulfate by CoO nanoparticles loaded on 3D mesoporous carbon nitride (CoO@ meso-CN) for the degradation of methylene blue (MB), Sci. Total Environ. 675 (2019) 531–541, https://doi.org/10.1016/j.scitotenv.2019.04.230.

[8] S. Arzate, S. Pfister, C. Oberschelp, J.A. Sánchez-Pérez, Environmental impacts of an advanced oxidation process as tertiary treatment in a wastewater treatment plant, Sci. Total Environ. 694 (2019) 133572, https://doi.org/10.1016/j.scitotenv.2019.07.378.

[9] A.K. Gaharwar, N.A. Peppas, A. Khademhosseini, Nanocomposite hydrogels for biomedical applications, Biotechnol. Bioeng. 111 (3) (2014) 441–453, https://doi.org/10.1002/bit.25160.

[10] B.D. Malhotra, M.A. Ali, Nanocomposite materials, *Nanomater. Biosens.* Elsevier (2018) 145–159, https://doi.org/10.1016/B978-0-323-44923-6.00005-4.

[11] R. Kumar, W. Dias, R.J.G. Rubira, A.V. Alaferdov, A.R. Vaz, R.K. Singh, S. R. Teixeira, C.J.L. Constantino, S.A. Moshkalev, Simple and fast approach for synthesis of reduced graphene oxide–MoS₂ hybrids for room temperature gas detection, IEEE Trans. Electron Devices 65 (9) (2018) 3943–3949, https://doi.org/10.1109/TED.2018.2851955.

[12] D.S. Rana, S. Kalia, N. Thakur, R.K. Singh, R. Kumar, D. Singh, Synthesis of reduced graphene oxide-molybdenum disulfide nanocomposite as potential scaffold for fabrication of efficient hydrazine sensor, Mater. Chem. Phys. 294 (2023) 127048, https://doi.org/10.1016/j.matchemphys.2022.127048.

[13] R. Wu, F. Zhang, X. Ji, Y. Liu, X. Guo, G. Tian, B. Liu, The mini-review for synthesis of core@Ag nanocomposite, Arab. J. Chem. 15 (1) (2022) 103519, https://doi.org/10.1016/j.arabjc.2021.103519.

[14] D. Yuan, M. Sun, S. Tang, Y. Zhang, Z. Wang, J. Qi, Y. Rao, Q. Zhang, All-solid-state BiVO₄/ZnIn₂S₄ Z-scheme composite with efficient charge separations for improved visible light photocatalytic organics degradation, Chin. Chem. Lett. 31 (2) (2020) 547–550, https://doi.org/10.1016/j.cclet.2019.09.051.

[15] S. Zhu, B. Dong, Y. Yu, L. Bu, J. Deng, S. Zhou, Heterogeneous catalysis of ozone using ordered mesoporous Fe₃O₄ for degradation of atrazine, Chem. Eng. J. 328 (2017) 527–535, https://doi.org/10.1016/j.cej.2017.07.083.

[16] B. Xu, H. Maimaiti, S. Wang, A. Awati, Y. Wang, J. Zhang, T. Chen, Preparation of coal-based graphene oxide/SiO₂ nanosheet and loading ZnO nanorod for photocatalytic Fenton-like reaction, Appl. Surf. Sci. 498 (2019) 143835, https://doi.org/10.1016/j.apsusc.2019.143835.

[17] C. Fu, M. Yan, Z. Wang, J. Li, X. Zhang, W. Song, Z. Xu, K. Bhatt, Z. Wang, S. Zhu, New insights into the degradation and detoxification of methylene blue using heterogeneous-Fenton catalyzed by sustainable siderite, Environ. Res. 216 (2023) 114819, https://doi.org/10.1016/j.envres.2022.114819.

[18] S. Ghosh, N.A. Kouamé, L. Ramos, S. Remita, A. Dazzi, A. Deniset-Besseau, P. Beaunier, F. Goubard, P.-H. Aubert, H. Remita, Conducting polymer nanostructures for photocatalysis under visible light, Nat. Mater. 14 (5) (2015) 505–511, https://doi.org/10.1038/nmat4220.

[19] D.S. Rana, S. Kalia, R. Kumar, N. Thakur, R.K. Singh, D. Singh, Two-dimensional layered reduced graphene oxide-tungsten disulphide nanocomposite for highly sensitive and selective determination of Para nitrophenol, Environ. Nanotechnol. Monit. Manage. 18 (2022) 100724, https://doi.org/10.1016/j.enmm.2022.100724.

[20] K. Maegawa, H. Nagai, R. Kumar, M.M. Abdel-Galeil, W.K. Tan, A. Matsuda, Development of polybenzimidazole modification with open-edges/porous-reduced graphene oxide composite membranes for excellent stability and improved PEM fuel cell performance, Mater. Chem. Phys. 294 (2023) 126994, https://doi.org/10.1016/j.matchemphys.2022.126994.

[21] R. Kumar, S. Sahoo, E. Joanni, R.K. Singh, R.M. Yadav, R.K. Verma, D.P. Singh, W. K. Tan, A. Pérez del Pino, S.A. Moshkalev, A. Matsuda, A review on synthesis of graphene, h-BN and MoS₂ for energy storage applications: Recent progress and perspectives, Nano Res. 12 (11) (2019) 2655–2694, https://doi.org/10.1007/s12274-019-2467-8.

[22] S. Kalia, R. Kumar, R. Sharma, S. Kumar, D. Singh, R.K. Singh, Two-dimensional layered rGO-MoS₂ heterostructures decorated with Fe₃O₄ nanoparticles as an electrochemical sensor for detection of Para-nitrophenol, J. Phys. Chem. Solid 184 (2024) 111719, https://doi.org/10.1016/j.jpcs.2023.111719.

[23] S. Kalia, D.S. Rana, N. Thakur, D. Singh, R. Kumar, R.K. Singh, Two-dimensional layered molybdenum disulfide (MoS₂)-reduced graphene oxide (rGO) heterostructures modified with Fe₃O₄ for electrochemical sensing of epinephrine, Mater. Chem. Phys. 287 (2022) 126274, https://doi.org/10.1016/j.matchemphys.2022.126274.

[24] M. Sohrabian, V. Mahdikhah, E. Alimohammadi, S. Sheibani, Improved photocatalytic performance of SrTiO₃ through a Z-scheme polymeric-perovskite

heterojunction with g-C$_3$N$_4$ and plasmonic resonance of Ag mediator, Appl. Surf. Sci. 618 (2023) 156682, https://doi.org/10.1016/j.apsusc.2023.156682.

[25] Q. Li, B. Guo, J. Yu, J. Ran, B. Zhang, H. Yan, J.R. Gong, Highly efficient visible-light-driven photocatalytic hydrogen production of CdS-cluster-decorated graphene nanosheets, J. Am. Chem. Soc. 133 (28) (2011) 10878–10884, https://doi.org/10.1021/ja2025454.

[26] Y. Dong, D.H. Son, Strongly nonlinear dependence of energy transfer rate on Sp^2 carbon content in reduced graphene oxide-quantum dot hybrid structures, J. Phys. Chem. Lett. 6 (1) (2015) 44–47, https://doi.org/10.1021/jz502414y.

[27] S.K. Ghosh, T. Pal, Interparticle coupling effect on the surface plasmon resonance of gold nanoparticles: From theory to applications, Chem. Rev. 107 (11) (2007) 4797–4862, https://doi.org/10.1021/cr0680282.

[28] V.S. Katta, V.R. Chappidi, S.S.K. Raavi, Plasmonic Au NPs embedded ytterbium-doped TiO$_2$ nanocomposites photoanodes for efficient indoor photovoltaic devices, Appl. Surf. Sci. 611 (2023) 155728, https://doi.org/10.1016/j.apsusc.2022.155728.

[29] T. Edvinsson, Optical quantum confinement and photocatalytic properties in two-, one- and zero-dimensional nanostructures, R. Soc. Open Sci. 5 (9) (2018) 180387, https://doi.org/10.1098/rsos.180387.

[30] D.S. Rana, S. Kalia, R. Kumar, N. Thakur, D. Singh, R.K. Singh, Microwave-assisted facile synthesis of layered reduced graphene oxide-tungsten disulfide sandwiched Fe$_3$O$_4$ nanocomposite as effective and sensitive sensor for detection of dopamine, Mater. Chem. Phys. 287 (2022) 126283, https://doi.org/10.1016/j.matchemphys.2022.126283.

[31] J. Zhao, M.A. Holmes, F.E. Osterloh, Quantum confinement controls photocatalysis: A free energy analysis for photocatalytic proton reduction at CdSe nanocrystals, ACS Nano 7 (5) (2013) 4316–4325, https://doi.org/10.1021/nn400826h.

[32] H.-Y. Kim, J.O. Sofo, D. Velegol, M.W. Cole, L.A.A. Van Der, Waals dispersion forces between dielectric nanoclusters, Langmuir 23 (4) (2007) 1735–1740, https://doi.org/10.1021/la061802w.

[33] C. Boerigter, R. Campana, M. Morabito, S. Linic, Evidence and implications of direct charge excitation as the dominant mechanism in plasmon-mediated photocatalysis, Nat. Commun. 7 (1) (2016) 10545, https://doi.org/10.1038/ncomms10545.

[34] E. Brillas, S. Garcia-Segura, Benchmarking recent advances and innovative technology approaches of Fenton, photo-Fenton, electro-Fenton, and related processes: A review on the relevance of phenol as model molecule, Sep. Purif. Technol. 237 (2020) 116337, https://doi.org/10.1016/j.seppur.2019.116337.

[35] M. Celentano, A. Jakhmola, P.A. Netti, R. Vecchione, Irreversible photo-Fenton-like triggered agglomeration of ultra-small gold nanoparticles capped with crosslinkable materials, Nanoscale Adv. 1 (6) (2019) 2146–2150, https://doi.org/10.1039/C8NA00353J.

[36] P. Kumar, U. Kumar, Y.-C. Huang, P.-Y. Tsai, C.-H. Liu, C.-H. Wu, W.-M. Huang, K.-L. Chen, Photocatalytic activity of a hydrothermally synthesized γ-Fe$_2$O$_3$@Au/MoS$_2$ heterostructure for organic dye degradation under green light, J. Photochem. Photobiol. A Chem. 433 (2022) 114186, https://doi.org/10.1016/j.jphotochem.2022.114186.

[37] X. Lin, X. Wang, Q. Zhou, C. Wen, S. Su, J. Xiang, P. Cheng, X. Hu, Y. Li, X. Wang, X. Gao, R. Nözel, G. Zhou, Z. Zhang, J. Liu, Magnetically recyclable MoS$_2$/Fe$_3$O$_4$ hybrid composite as visible light responsive photocatalyst with enhanced photocatalytic performance, ACS Sustainable Chem. Eng. 7 (1) (2019) 1673–1682, https://doi.org/10.1021/acssuschemeng.8b05440.

[38] K.-L. Chen, Z.-Y. Yang, C.-W. Lin, A magneto-optical biochip for rapid assay based on the cotton-mouton effect of γ-Fe$_2$O$_3$@Au Core/Shell nanoparticles, J. Nanobiotechnol. 19 (1) (2021) 301, https://doi.org/10.1186/s12951-021-01030-z.

[39] C.F. Holder, R.E. Schaak, Tutorial on powder X-ray diffraction for characterizing nanoscale materials, ACS Nano 13 (7) (2019) 7359–7365, https://doi.org/10.1021/acsnano.9b05157.

[40] Q. Chen, Y. Wang, K. Su, Q. Ma, Optical and electrical properties of Fe$_3$O$_4$@MoS$_2$ nanocomposites and doped Lead boron tellurite glass, Appl. Phys. A 125 (4) (2019) 284, https://doi.org/10.1007/s00339-019-2583-z.

[41] C.-W. Lin, J.-M. Chen, Y.-J. Lin, L.-W. Chao, S.-Y. Wei, C.-H. Wu, C.-C. Jeng, L.-M. Wang, K.-L. Chen, Magneto-optical characteristics of streptavidin-coated Fe$_3$O$_4$@Au Core-Shell nanoparticles for potential applications on biomedical assays, Sci Rep 9 (1) (2019) 16466, https://doi.org/10.1038/s41598-019-52773-7.

[42] Y. Hu, S. Lee, P. Kumar, Q. Nian, W. Wang, J. Irudayaraj, G.J. Cheng, Water flattens graphene wrinkles: Laser shock wrapping of graphene onto substrate-supported crystalline plasmonic nanoparticle arrays, Nanoscale 7 (47) (2015) 19885–19893, https://doi.org/10.1039/C5NR04810A.

[43] L. Tang, Y. Liu, G. Liu, Q. Chen, Y. Li, L. Shi, Z. Liu, X. Liu, A novel SERS substrate platform: Spatially stacking plasmonic hotspots films, Nanoscale Res. Lett. 14 (1) (2019) 94, https://doi.org/10.1186/s11671-019-2928-8.

[44] R.A. Bepari, P. Bharali, B.K. Das, Controlled synthesis of α- and γ-Fe$_2$O$_3$ nanoparticles via thermolysis of PVA gels and studies on α-Fe$_2$O$_3$ catalyzed styrene epoxidation, J. Saudi Chem. Soc. 21 (2017) S170–S178, https://doi.org/10.1016/j.jscs.2013.12.010.

[45] F. Maugé, J. Lamotte, N.S. Nesterenko, O. Manoilova, A.A. Tsyganenko, FT-IR study of surface properties of unsupported MoS$_2$, Catal. Today 70 (1) (2001) 271–284, https://doi.org/10.1016/S0920-5861(01)00423-0.

[46] L.A. Kolahalam, I.V. Kasi Viswanath, B.S. Diwakar, B. Govindh, V. Reddy, Y.L. N. Murthy, Review on nanomaterials: Synthesis and applications, Mater. Today:. Proc. 18 (2019) 2182–2190, https://doi.org/10.1016/j.matpr.2019.07.371.

[47] H.A. Alluhaybi, S.K. Ghoshal, B.O. Alsobhi, W.N. Wan Shamsuri, Visible photoluminescence from gold nanoparticles: A basic insight, Optik 192 (2019) 162936, https://doi.org/10.1016/j.ijleo.2019.162936.

[48] P. Hepperle, A. Herman, B. Khanbabaee, W.Y. Baek, H. Nettelbeck, H. Rabus, XPS examination of the chemical composition of PEGMUA-coated gold nanoparticles, Part. Part. Syst. Char. 39 (9) (2022) 2200070, https://doi.org/10.1002/ppsc.202200070.

[49] *Fast and large-area growth of uniform MoS2 monolayers on molybdenum foils - Nanoscale (RSC Publishing).* https://pubs.rsc.org/en/content/articlelanding/2016/nr/c5nr07226c (accessed 2024-01-29).

[50] L.R. Merte, J. Gustafson, M. Shipilin, C. Zhang, E. Lundgren, Redox behavior of iron at the surface of an O(100) single crystal studied by ambient-pressure photoelectron spectroscopy, Catal. Struct. React. 3 (1–2) (2017) 95–103, https://doi.org/10.1080/2055074X.2016.1275379.

[51] *One-pot co-precipitation synthesis of Fe3O4 nanoparticles embedded in 3D carbonaceous matrix as anode for lithium ion batteries | Journal of Materials Science.* https://link.springer.com/article/10.1007/s10853-018-3141-3 (accessed 2024-01-29).

[52] A. Sample, Y.-Y. He, Mechanisms and prevention of UV-induced melanoma, Photodermatol. Photoimmunol. Photomed. 34 (1) (2018) 13–24, https://doi.org/10.1111/phpp.12329.

[53] A.A. Okab, A.I. Alwared, A dual S-scheme g-C$_3$N$_4$/Fe$_3$O$_4$/Bi$_2$WO$_6$/Bi$_2$S$_3$ heterojunction for improved photocatalytic decomposition of methylene blue: Proposed mechanism, and stability studies, Mater. Sci. Semicond. Process. 153 (2023) 107196, https://doi.org/10.1016/j.mssp.2022.107196.

[54] W. Li, L. Shang, D. You, H. Li, H. Wang, L. Ma, X. Wang, Y. Li, Y. Li, Fabrication of Fe$_3$O$_4$@Ti-PDA nanoparticles with enhanced photocatalytic activities for degradation of organic dye, J. Phys. Chem. Solid 172 (2023) 111047, https://doi.org/10.1016/j.jpcs.2022.111047.

[55] P. Thi Lan Huong, N. Van Quang, N. Thi Huyen, H. Thu Huong, D. Anh Tuan, M. Trung Tran, Q. Vinh Tran, T. Ngoc Bach, N. Tu, V.-D. Dao, Efficiency enhancement of photocatalytic activity under UV and visible light irradiation using ZnO/Fe$_3$O$_4$ heteronanostructures, Sol. Energy 249 (2023) 712–724, https://doi.org/10.1016/j.solener.2022.12.011.

[56] P.M. Anjana, J.F. Joe Sherin, C. Vijayakumar, S.R. Sarath Kumar, M.R. Bindhu, R. B. Rakhi, Role of reduced graphene oxide-co-double-doped Fe$_3$O$_4$ nanocomposites for photocatalytic and supercapacitor applications, Mater. Sci. Eng. B 290 (2023) 116313, https://doi.org/10.1016/j.mseb.2023.116313.

[57] H. Ali, A.M. Ismail, Fabrication of magnetic Fe$_3$O$_4$/polypyrrole/carbon black nanocomposite for effective uptake of Congo Red and methylene blue dye: Adsorption investigation and mechanism, J. Polym. Environ. 31 (3) (2023) 976–998, https://doi.org/10.1007/s10924-022-02663-3.

[58] S. Selvaraj, M.K. Francis, P.B. Bhargav, N. Ahmed, Photocatalytic and antimicrobial performance evaluation of reusable MoS$_2$ nanoflowers under visible light, ECS Adv. 2 (1) (2023) 010502, https://doi.org/10.1149/2754-2734/acbc8c.

[59] M. Yu, D.R. Trinkle, Accurate and efficient algorithm for bader charge integration, J. Chem. Phys. 134 (6) (2011) 064111, https://doi.org/10.1063/1.3553716.

[60] O.I. Yanushevska, N.V. Vlasenko, G.M. Telbis, E.V. Leonenko, O.Z. Didenko, V. G. Prozorovich, A.I. Ivanets, T.A. Dontsova, Acid-Base and photocatalytic properties of TiO$_2$-based nanomaterials, Appl. Nanosci. 12 (3) (2022) 691–700, https://doi.org/10.1007/s13204-021-01709-7.

[61] L. Acharya, S.P. Pattnaik, A. Behera, R. Acharya, K. Parida, Exfoliated boron nitride (e-BN) tailored exfoliated graphitic carbon nitride (e-CN): an improved visible light mediated photocatalytic approach towards TCH degradation and H$_2$ evolution, Inorg. Chem. 60 (7) (2021) 5021–5033, https://doi.org/10.1021/acs.inorgchem.1c00062.

[62] Q. Li, B. Hu, Q. Yang, X. Cai, M. Nie, Y. Jin, L. Zhou, Y. Xu, Q. Pan, L. Fang, Interaction mechanism between multi-layered MoS$_2$ and H$_2$O$_2$ for self-generation of reactive oxygen species, Environ. Res. 191 (2020) 110227, https://doi.org/10.1016/j.envres.2020.110227.

[63] S. Wang, K. Wang, W. Cao, L. Qiao, X. Peng, D. Yu, S. Wang, C. Li, C. Wang, Degradation of methylene blue by ellipsoidal β-FeOOH@MnO$_2$ Core-Shell catalyst: Performance and mechanism, Appl. Surf. Sci. 619 (2023) 156667, https://doi.org/10.1016/j.apsusc.2023.156667.

[64] D. Wodka, R.P. Socha, E. Bielańska, M. Elżbieciak-Wodka, P. Nowak, P. Warszyński, Photocatalytic activity of titanium dioxide modified by Fe$_2$O$_3$ nanoparticles, Appl. Surf. Sci. 319 (2014) 173–180, https://doi.org/10.1016/j.apsusc.2014.08.010.

[65] J. Guo, C. Yang, Z. Sun, Z. Yang, L. Wang, C. Lu, Z. Ma, F. Guo, Ternary Fe$_3$O$_4$/MoS$_2$/BiVO$_4$ nanocomposites: Novel magnetically separable visible light-driven photocatalyst for efficiently degradation of antibiotic wastewater through p–n heterojunction, J Mater Sci: Mater Electron 31 (19) (2020) 16746–16758, https://doi.org/10.1007/s10854-020-04230-9.

[66] T. Ahmed, S. Balendhran, M.N. Karim, E.L.H. Mayes, M.R. Field, R. Ramanathan, M. Singh, V. Bansal, S. Sriram, M. Bhaskaran, S. Walia, Degradation of black phosphorus is contingent on UV–blue light exposure, NPJ 2D Mater. Appl. 1 (2017) 1–7, https://doi.org/10.1038/s41699-017-0023-5.

[67] Y. Li, J.G. DiStefano, A.A. Murthy, J.D. Cain, E.D. Hanson, Q. Li, F.C. Castro, X. Chen, V.P. Dravid, Superior plasmonic photodetectors based on Au@MoS$_2$ core-shell heterostructures, ACS Nano 11 (10) (2017) 10321–10329, https://doi.org/10.1021/acsnano.7b05071.

[68] S. Tang, M. Zhao, D. Yuan, X. Li, Z. Wang, X. Zhang, T. Jiao, J. Ke, Fe$_3$O$_4$ nanoparticles three-dimensional electro-peroxydisulfate for improving tetracycline degradation, Chemosphere 268 (2021) 129315, https://doi.org/10.1016/j.chemosphere.2020.129315.

[69] X. Yang, W. Chen, J. Huang, Y. Zhou, Y. Zhu, C. Li, Rapid degradation of methylene blue in a novel heterogeneous Fe_3O_4@rGO@TiO_2-catalyzed photo-Fenton system, Sci. Rep. 5 (1) (2015) 10632, https://doi.org/10.1038/srep10632.

[70] R. Vasquez-Medrano, D. Prato-Garcia, M. Vedrenne. Chapter 4 - Ferrioxalate-Mediated Processes. In *Advanced Oxidation Processes for Waste Water Treatment*; Ameta, S. C., Ameta, R., Eds.; Academic Press, 2018; pp 89–113. https://doi.org/10.1016/B978-0-12-810499-6.00004-8.

[71] Y. Cao, L. Guo, M. Dan, D.E. Doronkin, C. Han, Z. Rao, Y. Liu, J. Meng, Z. Huang, K. Zheng, P. Chen, F. Dong, Y. Zhou, Modulating electron density of vacancy site by single Au atom for effective CO_2 photoreduction, Nat. Commun. 12 (2021) 1675, https://doi.org/10.1038/s41467-021-21925-7.